Available online at www.sciencedirect.com
ScienceDirect
Journal of Power Sources 160 (2006) 1026–1034
JOURNAL OF POWER SOURCES
www.elsevier.com/locate/jpowsour

Two dimensional modeling study of PBI/H_3PO_4 high temperature PEMFCs based on electrochemical methods

Jingwei Hu, Huamin Zhang *, Jun Hu, Yunfeng Zhai, Baolian Yi

Dalian Institute of Chemical Physics, Chinese Academy of Sciences, PEMFC key materials and technology research group, Zhongshan Road 457#, Dalian, Liaoning Province 116023, China

Received 17 January 2006; received in revised form 13 February 2006; accepted 13 February 2006
Available online 31 March 2006

Abstract

A two dimensional model was constructed for a high temperature PBI/H_3PO_4 fuel cell, the model was focused on the cathode side since it is the most important component of the overall polarization loss in unit cell. Linear sweep voltammetry (LSV) technique was used to supply the model with the most important kinetic parameter—cathodic exchange current density. The cathode polarization was calculated by the resulting two dimensional model and the ohmic polarization was estimated by electrochemical impedance spectroscopy (EIS), the overall polarization curve was simulated according to the above procedure; three unit cells with different catalysts were assembled and their steady state polarization curves were simulated based on the mathematical model. Good agreement between the simulated and experimental results was achieved.

Keywords: H_3PO_4/PBI; High temperature; PEMFC; Two dimensional model; Cyclic voltametry; Electrochemical impedance spectroscopy

1. Introduction

Great success has been achieved with proton exchange fuel cells. Advanced features of this technology include: higher power density, environment friendly operation, all-solid construction and therefore reduced materials corrosion, but still some serious challenges, such as the catalytic activity when the operation temperature is below 80 °C; catalyst tend to be poisoned by impurities (CO, nitrides or sulfides) in the fuel stream; a major part of the water product is liquid and this can result in flooding of the electrode; still, if operated below 80 °C, the small difference between operational temperature and ambient temperature requires intensive cooling, especially when the ambient temperature is high or the cell is under high load. Recently, many researchers proposed different ways to solve the above problems, their efforts include developing high activity electro-catalysts to increase cell performance [1,2], improving the electrode structure for higher catalyst utilization [3], developing CO tolerant catalyst to alleviate catalyst poisonous effects [4] and proposing novel gas diffusion layers to reduce flooding [5], etc. However, there is a still long way to go before solving such problems satisfactorily, At the same time, researchers have turned to developing PEMFCs operated at higher temperature (above 120 °C). Different high temperature PEMFC systems have been proposed [6–9], as reviewed recently [10]. One system is the PBI/H_3PO_4 (phosphoric acid-doped polybenzimidazole) high temperature PEMFC. Researchers have focused their research work on its proton conductivity mechanism, catalyst activity and system integration [11–13]. However, modeling of the PBI/H_3PO_4 high temperature PEMFC is not well documented, Recently, Cheddie et al. [14,15] reported a one dimensional mathematic model of the high temperature PBI/H_3PO_4 system, but their study was limited. In this study, a two dimensional model based on electrochemical methods has been constructed, the LSV and EIS electrochemical techniques supplied to the model with the cathode exchange current density and cell internal resistance, generate good agreement between simulated and experimental results. Our model offers a new way to predict the performance of a PBI/H_3PO_4 high temperature PEMFC unit cell based on electrochemical techniques.

* Corresponding author. Tel.: +86 411 84379126; fax: +86 411 84665057.
E-mail address: zhanghm@dicp.ac.cn (H. Zhang).

0378-7753/$ – see front matter © 2006 Elsevier B.V. All rights reserved.
doi:10.1016/j.jpowsour.2006.02.026

Nomenclature

A	MEA active area
C	concentration
d	thickness
E	voltage
F	Faraday constant
i	current density
K	gas permeability
N	mass flux
Q	charge
R	universal gas constant
S	entropy
T	temperature
u	velocity

Greek letters

α	B–V coefficient
ε	gas porosity
γ	B–V coefficient
η	overpotential
μ	gas viscosity

2. Experimental

2.1. Electrode and MEA preparation

Catalyst mixtures were prepared by directly mixing TKK 46.2% Pt/C catalyst-cell A (TKK 29% Pt/C catalyst-cell B and J-M 20% Pt/C catalyst-cell C), NMP solution of PBI and PVDF. The mixtures were stirred thoroughly before they were applied to the wet-proofed carbon paper (SGL GDL 31 BC, 300 μm of thickness) by a tape-casting technique. The electrode fabrication was completed by drying at 80 °C for 2 h and 130 °C for 0.5 h in air. The platinum loading in the electrode of cells A–C was about 0.8 mg cm^{-2}, 0.75 mg cm^{-2} and 0.78 mg cm^{-2}, respectively. The same electrode was used both for the anode and the cathode. The PBI membrane (35 μm, provided by our international research partner) was first doped with 85% H_3PO_4 at 60 °C to obtain proton conduction. The unit cell was prepared as follows: firstly, the doped PBI membrane was sandwiched in between two electrodes, and then placed between two graphite plates with parallel gas channels. Two aluminum end plates with attached heaters were used to clamp the graphite plates by eight bolts with a torque of 3 N m. The active single cell area was 7.8 cm^2.

2.2. Polarization curves measurement

The unit cell was installed on a fuel cell test platform. The cell was operated at 150 °C, 0.2 MPa pressure (absolute pressure) was applied at both anode side and cathode side, and the flow rate was 100 mL s^{-1} over both sides. Since the gases were not humidified before entering the cell, the water content in the gas stream was negligible. The voltage was recorded when it reached steady state at different currents.

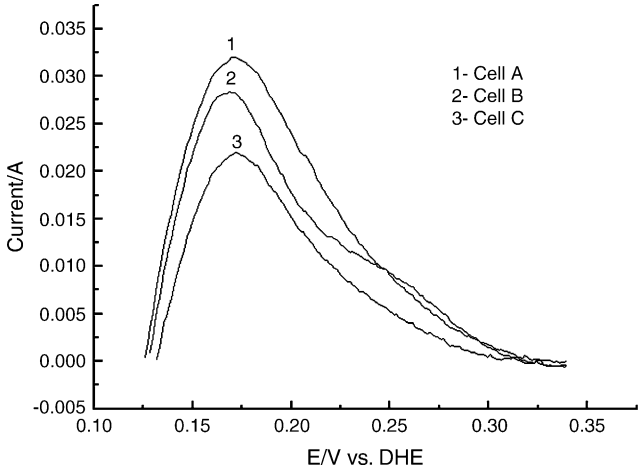

Fig. 2. Hydrogen desorption oxidation curves for unit cells.

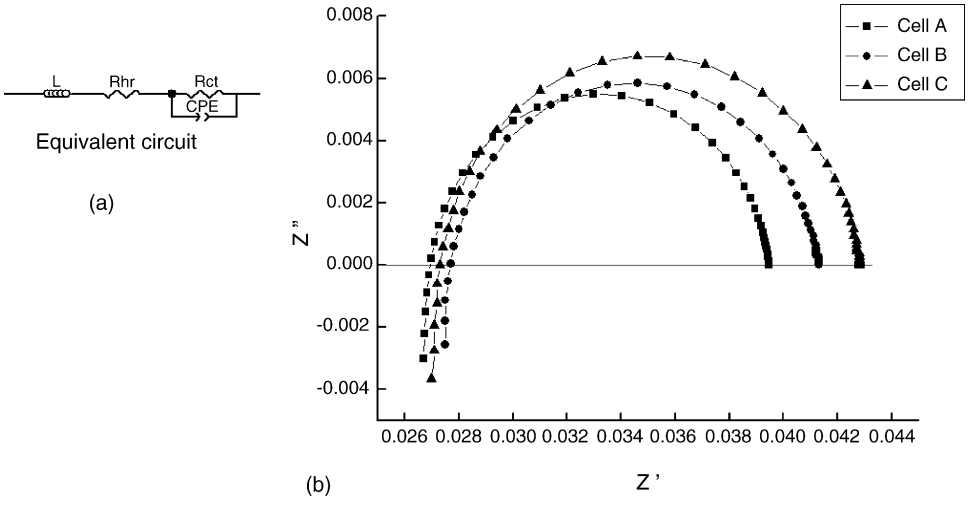

Fig. 1. (a) Equivalent circuit and (b) experimental (dots) and simulated (line) AC impedance diagrams for unit cells.

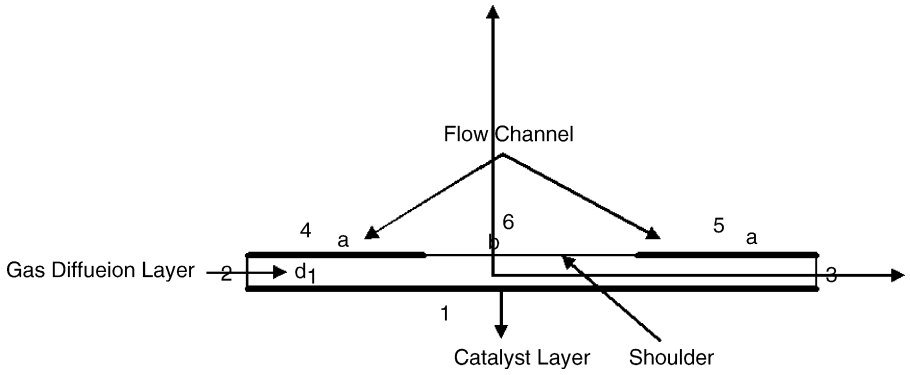

Fig. 3. The computational region. Half flow channel = 0.5 mm; width of shoulder = 1 mm; GDL thickness = 300 μm.

2.3. AC impedance measurement

The AC impedance measurement was conducted on the unit cell operated at constant load (600 mA cm^{-2}). The test frequency range was from 1 kHz to 100 mHz with logarithmic spacing and the AC amplitude was 10 mV. The electrochemical work station was an EG&G model 1025 FRA and model 263A. The equivalent circuit, measured AC impedance diagrams and equivalent circuit simulations are shown in Fig. 1(a and b). In the equivalent circuit shown in Fig. 1(a), L represents the inductance element; R_{hf} represents high frequency resistance that reflects the internal resistance of the unit cell; R_{ct} represents charge transfer resistance that reflects the resistance of chemical reaction, it is widely accepted that the anodic reaction resistance is negligible, so R_{ct} stands for the charge transfer resistance of cathodic reaction; CPE is the constant phase element that used to simulate the porous surface of the electrode. Fig. 1(b) shows that the simulated AC impedance results agree with the experimental data very well, so the proposed equivalent circuit in Fig. 1(a) is reasonable.

2.4. Unit cell LSV test

The LSV test was measured in a three-electrode configuration: WE was cathode side (purged by N_2 with flow rate of 100 mL s^{-1}), anode side acted as RE (DHE) and CE simultaneously (purged by H_2 with flow rate of 100 mL s^{-1}), the LSV curves were recorded from 0 V (versus DHE) to 0.6 V (versus DHE) with the scan rate of 20 mV s^{-1}. Typical unit cell LSV curves are listed in Fig. 2.

3. Model description

3.1. Model assumptions

The following assumptions are made in the development of the model:

(1) Steady state operation.
(2) Even temperature distribute in electrode.
(3) The reactant gases are ideal gases.
(4) Isotropic macro-homogeneous porous diffusion phase.
(5) Anode overpotential is omitted.
(6) Catalyst treated as interface rather than a region.

3.2. Computational region description

The computational region was showed in Fig. 3, as in Fig. 3, the cross region below two half flow channels and one shoulder was selected.

3.3. Brief introduction to govern equations

Overall voltage

$$E = E_r - \eta_{ohm} - \eta_c \quad (1)$$

Table 1
Physical parameters and basic conditions [14–17]

Items	Value
MEA active area A (cm^2)	7.8
EAS—electrochemical area surface (cm^2 mg^{-1} Pt)	As calculated
Active area factor, F_{area}	As calculated
Flow channel half width, a (m)	5×10^{-4}
Shoulder width, b (m)	10^{-3}
Oxygen molar concentration at flow channel, $C_{O_2,0}$ (mol m^{-3})	56.8
Water molar concentration at flow channel, $C_{H_2O,0}$ (mol m^{-3})	0
Oxygen reference concentration, $C_{O_2,ref}$ (mol m^{-3})	3.39
GDL thickness, d_1 (m)	3×10^{-4}
Catalyst layer thickness, d_2 (m)	5×10^{-5}
O_2 effective diffusion coefficient, $D^{eff}_{O_2}$ (m^2 s^{-1})	1.2×10^{-6}
Water effective diffusion coefficient, $D^{eff}_{H_2O}$ (m^2 s^{-1})	1.4×10^{-6}
Cathode permeability-coefficient, $k_{p,c}$ (m^2)	5.5×10^{-15}
ORR exchange current at planar Pt surface, $i_{0,area\text{-}planar}$ (A m^{-2})	10^{-3}
Volume exchange current, $i_{0,volume}$ (A m^{-3})	As calculated
Working pressure, P (Pa)	2×10^5
High frequency resistance (internal resistance), R_{hf} (Ω cm^{-2})	As measured
Working temperature, T (K)	423
Cathode porosity, ε_c	0.4
Pt loading, L_{Pt} (mg cm^{-2})	1
Cathode gas viscosity, μ_c (kg m^{-1} s^{-1})	2×10^{-5}
Hydrogen atom absorption factor: Q_{ref} (μQ cm^{-2})	220
α_a	0.5
α_c	1
γ_c	1

$$\eta_{\text{ohm}} = I \cdot R_{\text{hf}} \tag{2}$$

where R_{hf} can be determined by EIS

$$E_{\text{r}} = E_{\text{r}}^{0} + \frac{\Delta S}{nF} \cdot (T - T_0) + \frac{2RT}{nF} \cdot \ln\left(P_{\text{H}_2} \cdot \frac{P_{\text{O}_2}^{0.5}}{P_{\text{w}}}\right) \tag{3}$$

where reversible cell potential is 1.185 at $T = T_0 = 298$ K and reactant gases at its standard conditions.

The following relation is valid for 400 K < T < 500 K:

$$\frac{\Delta S}{n} = -18.449 - 0.01283 \cdot T \tag{4}$$

In cathode diffusion layer

$$\nabla \vec{N}_{\text{O}_2} = 0 \tag{5}$$

$$\nabla \vec{N}_{\text{H}_2\text{O}} = 0 \tag{6}$$

The mass flux of oxygen and gaseous water can be divided into two terms as:

$$\vec{N}_{\text{O}_2} = -\varepsilon D_{\text{O}_2}^{\text{eff}} \nabla C_{\text{O}_2} + \varepsilon C_{\text{O}_2} \vec{u} \tag{7}$$

$$\vec{N}_{\text{H}_2\text{O}} = -\varepsilon D_{\text{H}_2\text{O}}^{\text{eff}} \nabla C_{\text{H}_2\text{O}} + \varepsilon C_{\text{H}_2\text{O}} \vec{u} \tag{8}$$

The first term $-\varepsilon D^{\text{eff}} \nabla C$ in Eqs. (7) and (8) represents diffusion flux and the second term $\varepsilon C\vec{u}$ in Eq. (7) and (8) represents convection flux.

If combined Darcy law-equation (9) which is typically used to descript porous diffusion media into Eqs. (7) and (8), Eqs. (5) and (6) can be written in the form as Eqs. (10) and (11)

$$\vec{u} = -\frac{k_{\text{p}} RT}{\mu} \nabla (C_{\text{O}_2} + C_{\text{H}_2\text{O}}) \tag{9}$$

$$\nabla \left(-\varepsilon D_{\text{O}_2}^{\text{eff}} \nabla C_{\text{O}_2} - \frac{\varepsilon C_{\text{O}_2} k_{\text{p}} RT}{\mu} \nabla (C_{\text{O}_2} + C_{\text{H}_2\text{O}})\right) = 0 \tag{10}$$

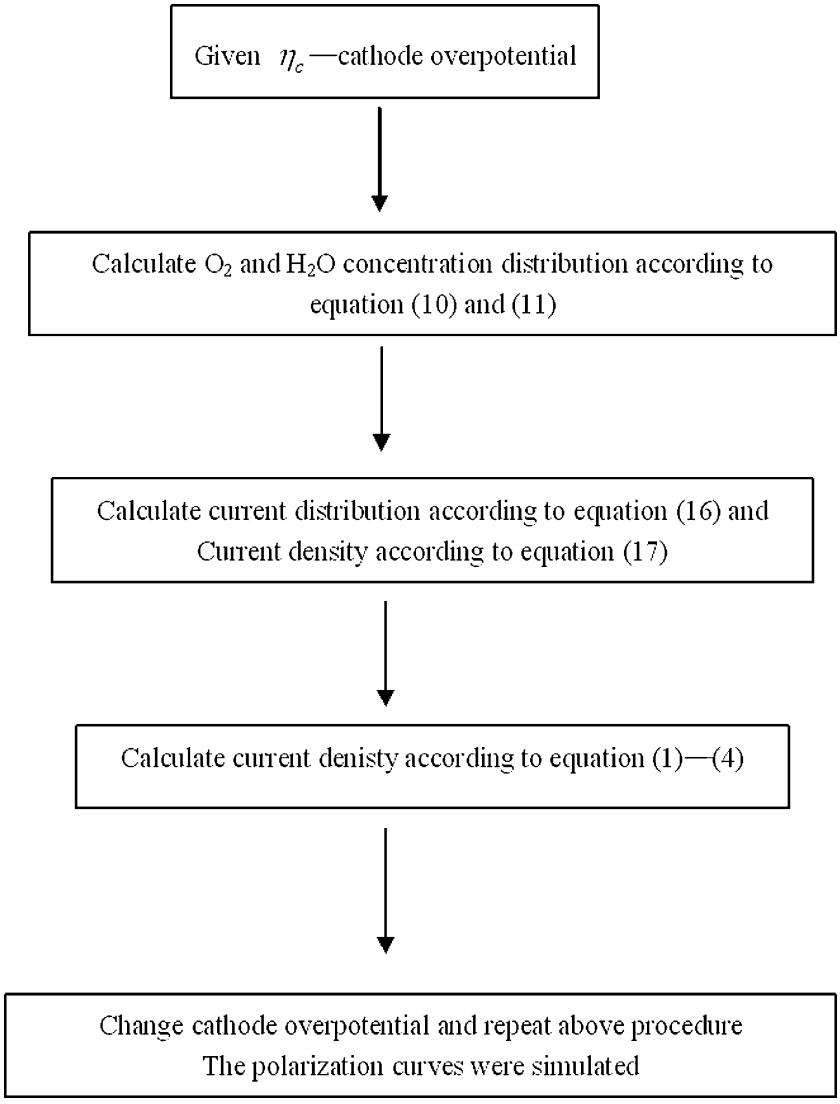

Fig. 4. Solution algorithm.

$$\nabla\left(-\varepsilon D_{H_2O}^{eff}\nabla C_{H_2O} - \frac{\varepsilon C_{H_2O} k_p RT}{\mu}\nabla(C_{O_2} + C_{H_2O})\right) = 0 \quad (11)$$

3.4. Boundary conditions

Boundaries 2 and 3 are symmetric interface, so the mass flux at normal direction of O_2 and H_2O is zero:

$$\vec{N}_{O_2,n} = 0; \quad \vec{N}_{H_2O,n} = 0 \quad (12)$$

Boundaries 4 and 5 are the interface between flow channel and GDL, so the constant concentration is applied as:

$$C_{O_2} = C_{O_2,0}; \quad C_{H_2O} = C_{H_2O,0} \quad (13)$$

Boundary 6 is the interface below shoulder, the mass flux at normal direction of O_2 and H_2O is zero:

$$\vec{N}_{O_2,n} = 0; \quad \vec{N}_{H_2O,n} = 0 \quad (14)$$

Boundary 1 is the catalyst layer interface, where oxygen is consumed and water is formed, so the boundary conditions can be described as below combined with the general accepted electrochemical B–V Eq. (16):

$$\vec{N}_{O_2,n} = -\frac{I'}{4F}; \quad \vec{N}_{H_2O,n} = \frac{I'}{2F} \quad (15)$$

Table 2
Cathode volume exchange current density for unit cells

	Cell number		
	Cell A	Cell B	Cell C
Cathode volume exchange current density ($A\,m^{-3}$)	1649	1404.4	996

Table 3
Internal resistance for unit cells

	Cell number		
	Cell A	Cell B	Cell C
Internal resistance ($\Omega\,cm^2$)	0.209	0.218	0.21

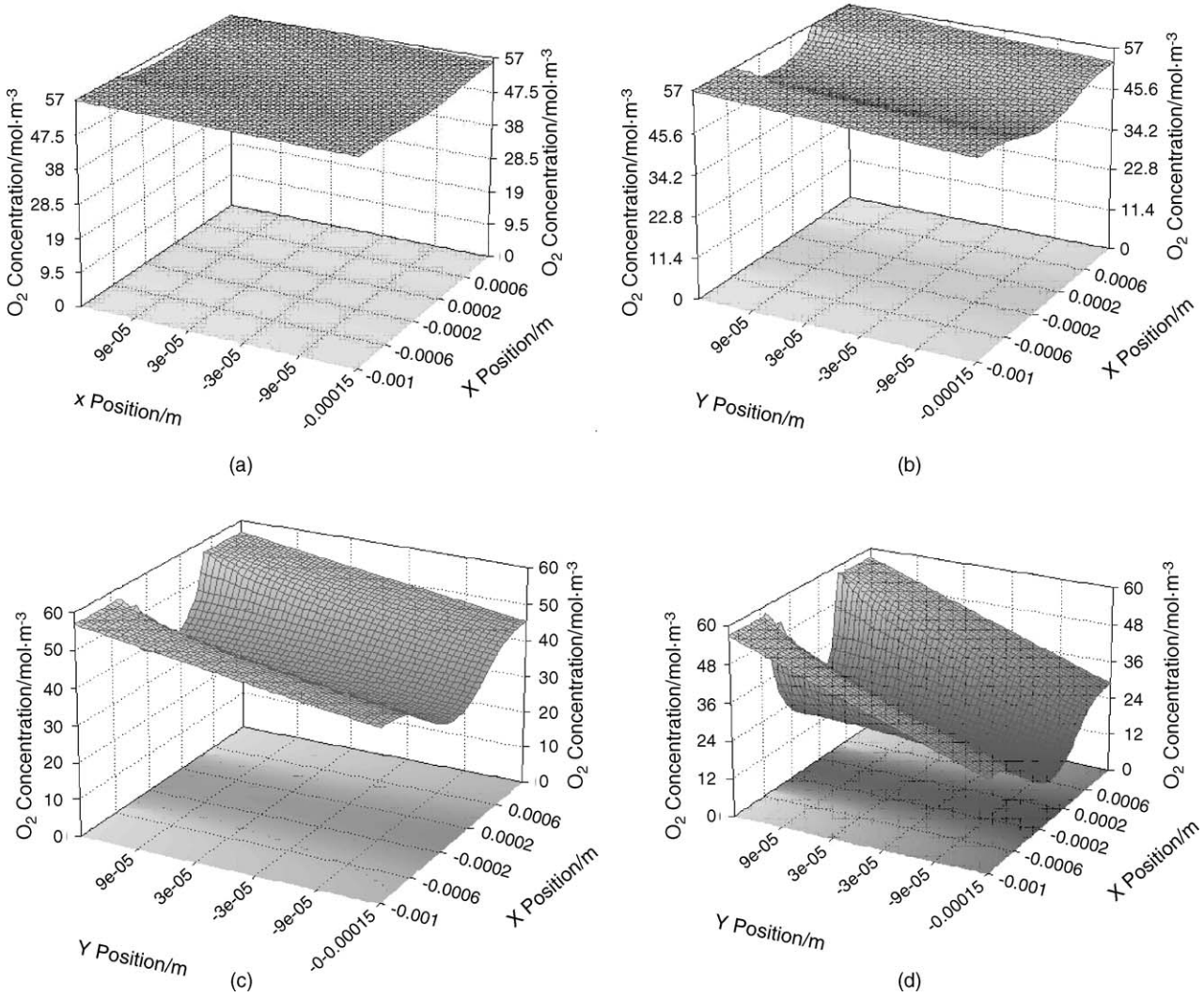

Fig. 5. Oxygen concentration surface plots at different cathode overpotentials for cell A: (a) $\eta_c = 0.05$ V; (b) $\eta_c = 0.15$ V; (c) $\eta_c = 0.25$ V; (d) $\eta_c = 0.35$ V.

where

$$I' = i_{0,\text{area}} \cdot \left(\frac{C_{O_2}}{C_{O_2,\text{ref}}}\right)^{\gamma_c} \cdot \left[\exp\left(\frac{\alpha_c F\eta_c}{RT}\right) - \exp\left(-\frac{\alpha_a F\eta_c}{RT}\right)\right] \quad (16)$$

3.5. Numerical values

The operating conditions and electrode parameters are shown in Table 1.

3.6. Solution algorithm

Fig. 4 shows the solution algorithm used. After the current density along the catalyst layer is obtained, the current density can be calculated by the following:

$$I = L^{-1} \cdot \int_0^L I' \, dx \quad (17)$$

According to the solution algorithm showed in Fig. 4, the polarization curves can be simulated. The equations of this model were solved using commercially available program FEMLAB®.

3.7. Parameters derived from electrochemical measurements

The cathode volume exchange current density was calculated according to the following:

$$\text{EAS} = \frac{Q_H}{Q_{\text{ref}} \cdot L_{\text{pt}} \cdot A} \quad (18)$$

$$F_{\text{area}} = \text{EAS} \cdot L_{\text{pt}} \quad (19)$$

$$i_{0,\text{area}} = \text{EAS} \cdot L_{\text{pt}} \cdot i_{0,\text{area-planar}} \quad (20)$$

$$i_{0,\text{volume}} = \text{EAS} \cdot L_{\text{pt}} \cdot i_{0,\text{area-planar}} \cdot d_2^{-1} \quad (21)$$

Eq. (19) gives the active area factor that represents the ratio between electrochemical area surface and apparent electrode

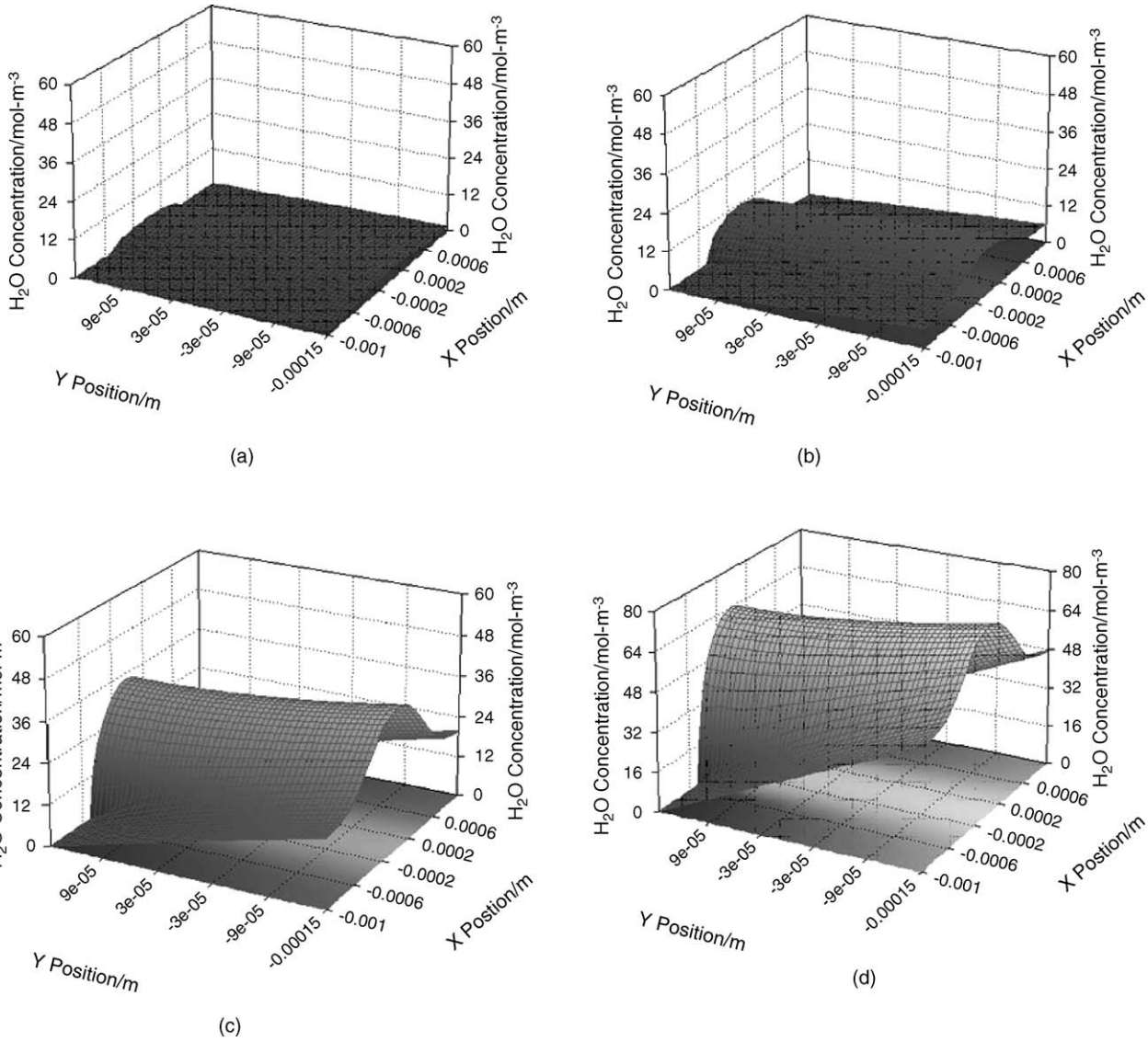

Fig. 6. Gaseous water concentration surface plots at different cathode overpotentials for cell A: (a) $\eta_c = 0.05$ V; (b) $\eta_c = 0.15$ V; (c) $\eta_c = 0.25$ V; (d)$\eta_c = 035$ V.

area; Eqs. (20) and (21) give the cathode area exchange current density and volume exchange current density respectively. The calculated cathode volume exchange current densities for different unit cells are shown in Table 2. The electrochemical method offers a new way to determine the cathode area exchange current density and volume exchange current density, the value of calculated cathode volume exchange current density is comparable to that generally cited in literature [17]—440 A m^{-3}.

As to cell internal resistance, the value was determined by the AC impedance measurement based on equivalent circuit analysis, no obvious mass transfer resistance related to the transfer phenomenon caused by liquid water [18] in the lower frequency region was found and no liquid water exists in the high temperature PEMFCs, only the internal resistance R_{hf} and the charge transfer resistance R_{ct} appear in the AC impedance diagram, so it is reasonable to assume that ohmic polarization and cathode reaction polarization are the main contributions to the polarization, as is shown in Eq. (1).

The R_{hf} for different cells is listed in Table 3. It should be noted that the R_{hf} in Table 3 is the internal resistance when the cell is operated at the current density of 600 mA cm^{-2}, in general, the R_{hf} dependence on current density should be measured for R_{hf} is dependant on current density, however, in our experiment, we found that the internal resistance derived from AC impedance is almost stable when changing the load, we attribute this phenomenon to the proton conduction of PBI/H_3PO_4 membrane which is independent of the water content. For this reason, the internal resistance of the unit cell is taken as a constant.

4. Simulation results

Fig. 5(a–d) list the O_2 concentration distributions at different cathode overpotentials for cell A (cell B and cell C have similar results that is omitted here) in GDL based on the two dimensional model described above, from Fig. 5, the O_2 concentration of the region near catalyst layer is lower than that near flow channel for O_2 is consumed at catalyst layer; and the O_2 concentration gradient increases with increase of cathode overpotential, the mean O_2 concentration at the catalyst layer decreases to 21.9 when the cathode overpotential is 0.35 V (Fig. 5(d)); in addition, the O_2 concentration of the GDL region under shoulder ($-0.5\,mm \leq x \geq 0.5\,mm$) is lower than that of the GDL region under the flow channel for the GDL region since O_2 can only enter this region from the X direction.

Fig. 6(a–d) list the gaseous water concentration distributions at different cathode overpotentials for cell A based on the two dimensional model (cells B and C have similar results but are omitted here), from Fig. 6, the gaseous water concen-

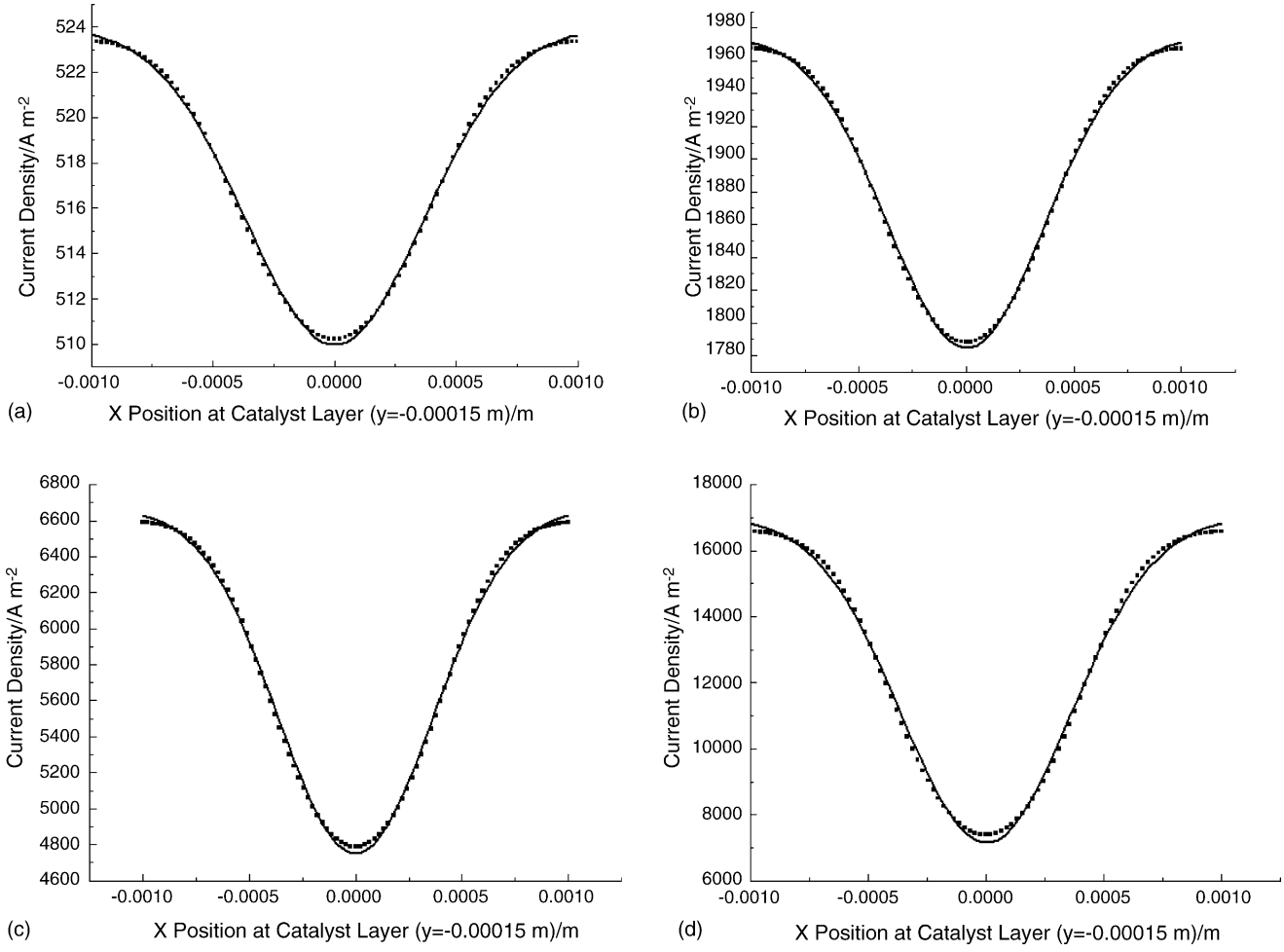

Fig. 7. Current density distributions at catalyst interface at different cathode overpotentials for cell A: (a) $\eta_c = 0.05$ V; (b) $\eta_c = 0.15$ V; (c) $\eta_c = 0.25$ V; (d) $\eta_c = 0.35$ V.

Table 4
Current density under shoulder and under flow channel at different cathode overpotential

	Cathode overpotential			
	0.05	0.15	0.25	0.35
Mean current density under shoulder (A cm^{-2})	0.0513	0.183	0.522	0.960
Mean current density under flow channel (A cm^{-2})	0.0521	0.195	0.689	1.560

tration of the region near catalyst layer is higher than that of the region near flow channel for water that is produced by the catalyst layer; and the water concentration gradient also increases with increase of cathode overpotential. In addition, the water concentration of the GDL region under the shoulder is higher than that of the GDL region under the flow channel because the transport of water produced at the catalyst layer is blocked by the shoulder that does not contact the flow channel directly.

Fig. 7(a–d) show the current density distributions along the catalyst layer for cell A at different cathode overpotentials, also the equivalent plots of cell B and cell C are omitted in this paper for brevity. The solid line in Fig. 7 represents the Gaussian fit of the current density distribution along the catalyst layer, and the obtained continuous fitted line is used to calculate the mean current density along catalyst layer according to Eq. (17). From Fig. 7 the current density distributions along catalyst layer are proportional to the O_2 concentration distribution along the catalyst layer (please refer to Fig. 5), and the current density at the catalyst layer under the shoulder is lower than that under the flow channel, this effect is more obvious when the cathode overpotential increases (Table 4). For this reason, the catalyst under the shoulder is not fully utilized especially when the cathode overpotential is high.

Fig. 8(a–c) show the experimental and simulated polarization curves in this study, from Fig. 8, the experimental and simulated

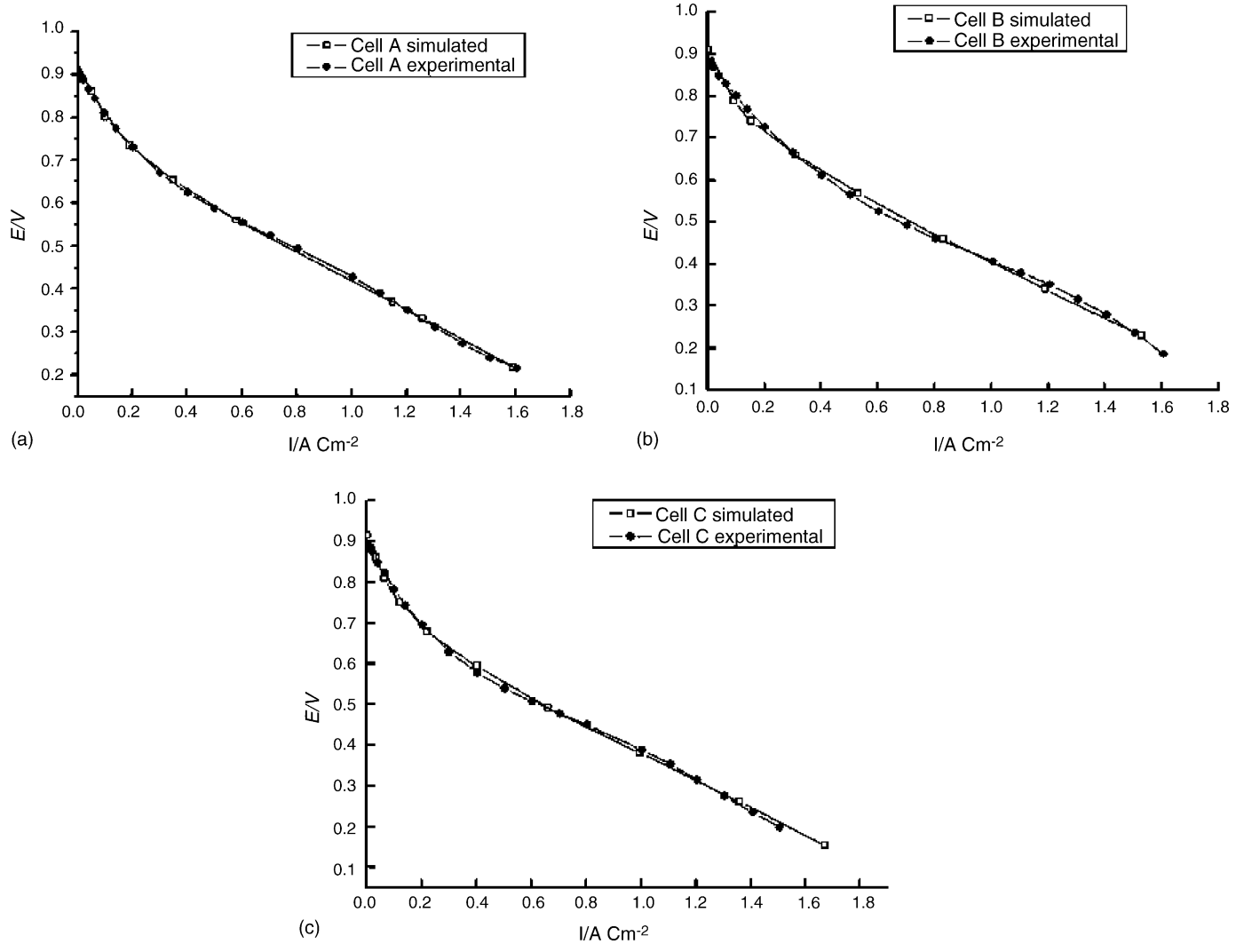

Fig. 8. Experimental and simulated polarization curves: (a) cell A; (b) cell B; (c) cell C.

results agree with each other very well, which verifies the reliability of our model.

It should be noted that this model is a preliminary two dimensional model study of the PBI/H_3PO_4 high temperature PEMFC fuel cell, and the catalyst layer is treated as a reaction interface, so it cannot reflect the effect of catalyst microstructure on the cell performance, more detailed model research work combined with electrochemical techniques is under development in our group.

5. Conclusion

A two dimensional cathode model combined with electrochemical data was constructed in this study based on the PBI/H_3PO_4 high temperature PEMFC fuel cell, the oxygen and gaseous water concentration distributions were calculated based on the model, the polarization curves of three unit cells were simulated, and the simulated and experimental results agree well.

Acknowledgements

The authors wish to express their thanks to the National Natural Science Foundation of China (PR China, Grant No. Grant No. 50236010).

References

[1] N. Lebedeva, P.J.M. Janssen, Electrochim. Acta 51 (2005) 29–40.
[2] B. Wang, J. Power Sources 152 (2005) 1–15.
[3] R. Fernández, P.F. Aparicio, L. Daza, J. Power Sources 151 (2005) 18–24.
[4] N.P.G. Lebedeva, J.M. Janssen, Electrochim. Acta 51 (2005) 29–40.
[5] Y. Bultel, K. Wiezell, F. Jaouen, Electrochim. Acta 151 (2005) 474–488.
[6] J.H. Chen, T. Matsuura, M. Hori, J. Power Sources 131 (2004) 155–161.
[7] W.H.J. Hogarth, J.C. Costa, G.Q. Lu, J. Power Sources 142 (2005) 223–237.
[8] Y.T. Kim, M.K. Song, K.H. Kim, Electrochim. Acta 50 (2004) 645–648.
[9] S.H. Kwak, T.H. Yang, C.S. Kim, Electrochim. Acta 50 (2004) 653–657.
[10] Y.M. Kim, S.H. Choi, H.C. Lee, Electrochim. Acta 49 (2004) 4787–4796.
[11] Q.F. Li, R.H. He, R.W. Berg, Solid State Ionics 168 (2004) 177–185.
[12] R.H. He, Q.F. Li, G. Xiao, J. Membr. Sci. 226 (2003) 169–184.
[13] Q.F. Li, H.A. Hjuler, N.J. Bjerrum, Electrochim. Acta 45 (2000) 4219–4226.
[14] D. Cheddie, N. Munroe, Energy Conversion and Management 47 (2006) 1490–1504.
[15] D. Cheddie, N. Munroe, J. Power Sources 160 (2006) 215–223.
[16] W. Sun, B.A. Peppley, K. Karan, J. Power Sources 144 (2005) 42–45.
[17] G. Hu, J. Fan, S. Chen, J. Power Sources 136 (2004) 1–9.
[18] Z. Xie, S. Holdcroft, J. Electroanal. Chem. 568 (2004) 247–260.